JOURNAL OF MATERIALS SCIENCE 30 (1995) 869–878

Effect of microstructural coarsening on Hertzian contact damage in silicon nitride

HOCKIN H. K. XU*, LANHUA WEI‡, NITIN P. PADTURE§, B. R. LAWN
Materials Science and Engineering Laboratory, National Institute of Standards and Technology, Gaithersburg, MD 20899, USA

R. L. YECKLEY
Norton/TRW Ceramics, Northboro, MA 01532, USA

The critical role of grain size in determining the nature of damage accumulation in silicon-nitride ceramics is evaluated using Hertzian contact testing. Single-cycle tests are conducted on materials of two grain sizes, 0.5 μm (fine) and 2.0 μm (coarse). Damage patterns for these two materials are compared and contrasted using a special bonded-interface specimen to investigate the subsurface regions. Optical and thermal wave-imaging techniques provide complementary pictures of the damage patterns: whereas the optical image maps elements of both deformation and fracture, the thermal wave image maps only the fracture. Taken together, these two imaging methods disclose a fundamental transition in the mechanical response in the two silicon nitrides, from cone-crack-dominated in the fine material to distributed-microcrack-dominated in the coarse material. Scanning electron microscopy (SEM) confirms the incidence of microfracture in the latter case. Thermal-wave measurements also allow a quantitative evaluation of the microfracture damage. Multiple-cycle tests on the coarse material show a build up of subsurface damage with increasing number of cycles, indicating mechanical fatigue. The results are discussed in terms of a shear-fault model, in which subsurface microcracks initiate from intrinsic planes of shear weakness in the microstructure. Implications concerning the microstructural design of silicon nitride ceramics for strength and wear applications are briefly considered, with reference to countervailing resisting and driving forces in the long-crack and short-crack toughness characteristics.

1. Introduction

Structural ceramics are now being used in bearings, valves, rotors, engine parts and other applications where damage resistance is a major consideration [1]. Many of these applications involve severe contact stresses. Toughness is a governing factor in damage resistance, particularly at the grain level where many contact-related microfracture processes operate. In polycrystalline ceramics, there is a tendency as revealed by indentation–strength studies [2–5], to inverse relations in the short-crack and long-crack toughness values. This is because the same weak interfaces, coarse grains and internal stresses that enhance the resistance of large cracks, by grain bridging [2, 4–11], conversely diminish the resistance of short cracks, by providing easy fracture paths along tensile grain facets [4, 5]. Consequently, the use of traditional long-crack testing methodologies for characterizing toughness is open to question. Nowhere is this more so than in the fatigue properties in repeat contact loading of apparently perfectly finished components where ultimate failures originate at the sub-grain level.

Of those practical ceramics considered for contact applications, silicon nitride is especially important because of its intrinsically high toughness [1]. Again, microstructure is a critical element of the toughness in this material. It has been demonstrated in the *in-situ*-processing studies of Li *et al.* [12, 13] that grain coarsening and elongation enhances long-crack toughness but diminishes the laboratory strength of silicon nitride. However, quantitative evaluations of the damage and fatigue resistance at stress concentrations in relation to the microstructure, specifically in

* Guest Scientist, on leave from Department of Materials Science and Engineering, University of Maryland, College Park, MD 20742, USA.
‡ Guest Scientist, on leave from Department of Physics and Astronomy, Wayne State University, Detroit, MI 48201, USA.
§ Guest Scientist, on leave from Department of Materials Science and Engineering, Lehigh University, Bethlehem, PA 18015, USA; now with Department of Metallurgy and Institute of Materials Science, University of Connecticut, Storrs, CT 06269, USA.

0022–2461 © *1995 Chapman & Hall*

terms of short-crack toughness behaviour, have yet to be made.

A test methodology based on the classical Hertzian-contact geometry is now available for such evaluations [14–17]. The test itself is simple to perform and economical in specimen preparation, and simulates the essential features of many practical contact problems. Data obtained on alumina highlight the crucial role of microstructural variation, specifically grain size, on the damage and fatigue characteristics [15]. In that alumina, a fundamental transition is observed in the Hertzian damage pattern, from the classical tensile-driven cone fracture [18] in fine-grained material to distributed shear-driven, subsurface microfracture damage in coarse-grained material. Some studies of subsurface contact damage using conical indenters have foreshadowed a similar kind of microstructure-determined transition in silicon nitride [19–21]. However, conical indenters are limited by their fixed profile to a constant contact pressure (the *indentation hardness* [22]), and thus do not have the same capacity as spherical indenters to investigate the initial stages of damage evolution within the contact field. This is one limitation the present study seeks to redress.

Accordingly, we examine damage accumulation patterns in single-cycle and in multi-cycle Hertzian-contact loading in fine-grained and coarse-grained silicon nitride. Optical and thermal-wave methodologies are used as complementary techniques to characterize and quantify the damage. It will be shown that the scale of the microstructure is decisive, resulting in a significant shift from single cone crack to distributed microfracture damage as grain size is increased. To establish a base for interpreting this shift, conventional indentation–strength tests using Vickers indenters are used to characterize the strength characteristics over the short-crack/long-crack domain [23]. The results have important implications for microstructural tailoring of silicon nitride materials for specific applications.

2. Experimental procedure

Silicon nitrides in two grain sizes were selected for study. These materials were yttria-doped (4 vol %) and were hot-isostatically pressed. Heat treatments were controlled so that elongated grains were produced with an aspect ratio of 4–5, and widths of 0.5 μm (*fine-grained material*) and 2.0 μm (*coarse-grained material*). The materials had α and β phases in the ratios 30/70 for the fine-grained material and 0/100 for the coarse-grained material. Both contained a residual grain-boundary phase (notably at triple-point junctions), and had a porosity of less than 1%. The Vickers indentation hardnesses, 20.0 GPa (fine-grained material) and 16.3 GPa (coarse-grained material), reflect the relative hardnesses of the α and β phases.

Bars with dimensions 25 × 4 × 3 mm for the strength tests were polished to 1 μm diamond-paste finish, with chamfered edges to avoid edge failures. A Vickers indenter was used to introduce controlled radial cracks into the centres of each of the test specimens, at peak loads in the range 2–300 N. These specimens were broken in four-point flexure, with the indented surface on the tensile side. Inert strengths were measured at fast stressing rates ($\sim 1000\ \mathrm{MPa\,s^{-1}}$) in inert (oil) environment.

Hertzian contact damage experiments were conducted on similar bar specimens, using tungsten carbide spheres of radius 1.98 mm. Some tests were made on surfaces pre-coated with a thin film of soft metal so that the contact pressure could be evaluated from the area of the contact impression and the peak load [14]. Most tests, however, were made using the bonded-interface configuration shown in Fig. 1 [15], to provide information on subsurface damage. These latter specimens were prepared by bonding two edge-polished rectangular half-blocks together with a thin (< 1 μm) layer of adhesive. Indentations were made symmetrically across the trace of the bonded interface on the polished top surface. The specimens were then immersed in a solvent to dissolve the adhesive and expose the section beneath the indentations. Single-cycle tests were conducted at slow loading rates, typically over a period of ~ 100 s. Preliminary runs revealed no dependence of loading period down to ~ 0.1 s, indicating that no significant slow crack growth had occurred. Repeat-load tests were run at a frequency of 10 Hz. The indented surfaces and sections were coated with a thin layer of gold and were viewed with an optical microscope in Nomarski illumination to reveal the macroscopic damage patterns. Higher-magnification views were obtained by scanning electron microscopy (SEM).

Additional views of the macroscopic damage patterns were obtained by thermal-wave imaging, using the set-up shown in Fig. 2 [24, 25]. Surfaces and sections of indented, gold-coated specimen surfaces were irradiated with a chopped argon-ion laser heating beam, over a spot of diameter ~ 20 μm, and were

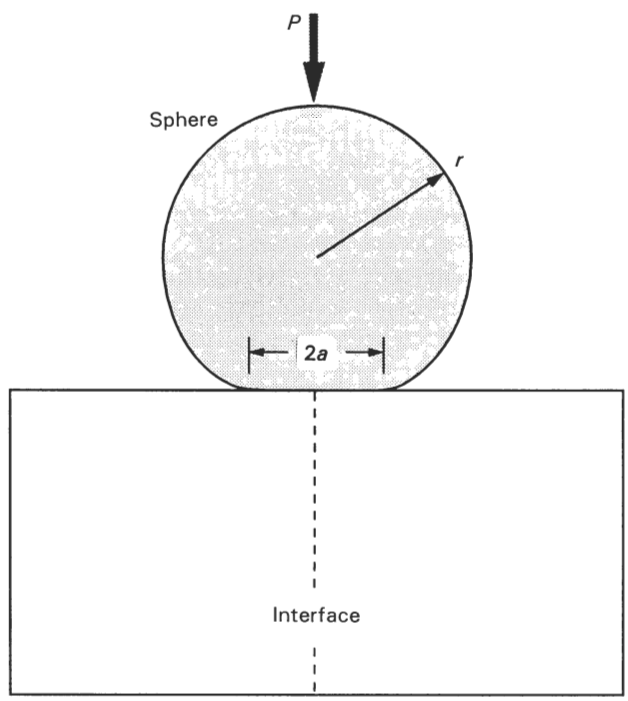

Figure 1 Schematic of bonded-interface specimen used in the contact-damage experiment. (Redrawn, with permission, from [15].)

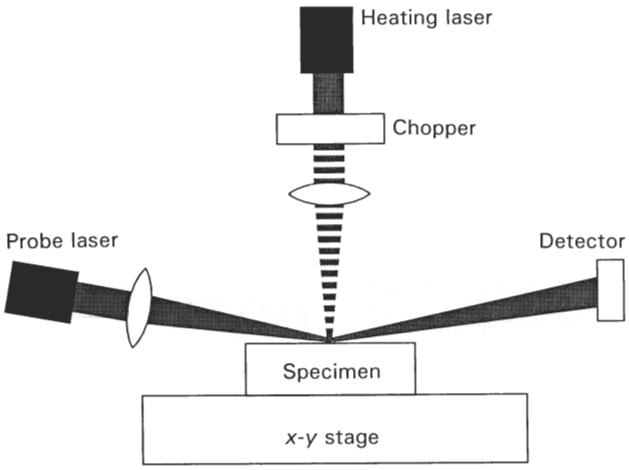

Figure 2 Schematic of thermal-wave set-up, using a mirage effect to determine local variations in thermal diffusivity at the specimen near-surface. (Redrawn, with permission, from [25].)

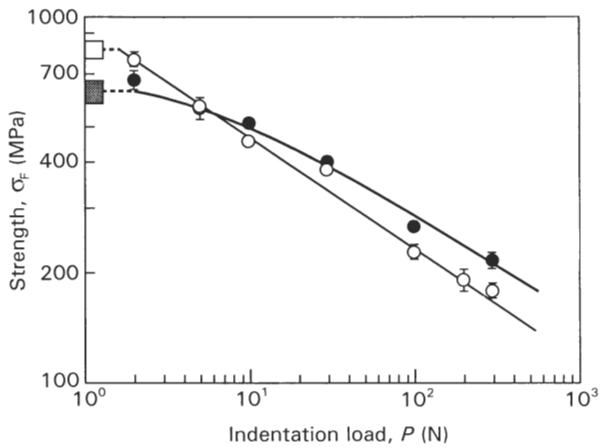

Figure 3 Indentation-strength data for: (○) fine- and (●) coarse-grained silicon nitride. Each data point and bar represents the mean and standard deviation of breaks from 3–5 specimens. Squares at left are laboratory strengths.

scanned with a helium–neon laser probe beam at grazing incidence. The intermittent heating produces periodic spatial and temporal fluctuations (thermal waves) in the irradiated specimen surfaces. The degree of local heating is highly sensitive to the diffusivity conditions in the irradiated specimen volume. The heated material in turn heats the immediately surrounding atmosphere. Accordingly, variations in the specimen near-surface diffusivity conditions can be monitored by a detector which locates the position of the refracted probe beam ("mirage" effect). In our experiments, the set-up was operated in two modes: (i) an imaging mode (chopping frequency 100 Hz, corresponding to a thermal penetration depth ~ 300 μm), in which the specimen is scanned through the two fixed beams using a stepping motor and the probe beam deflection is recorded on a data-acquisition system to produce a thermal image [25]; (ii) a diffusivity mode (chopping frequency 500–5000 Hz, thermal decay depth ~ 40–140 μm), in which the heating beam is held fixed relative to the specimen and the probe beam is scanned, allowing the material diffusivity to be evaluated within the heated volume (radius $\approx$ thermal-decay depth) below the irradiated spot [24, 25].

3. Results

3.1. Indentation–strength results

Data for strength, σ_F, as a function of Vickers-indentation peak load, P, are plotted for the fine-grained and coarse-grained silicon nitrides in Fig. 3. The data points are means and standard deviations (error bars) for breaks from indentation sites. The solid curves are empirical fits through these data points.

Note that the curves for the two materials cross. Thus, whereas the fine-grained material is stronger in the low-load (short-crack) region, the coarse-grained material is stronger in the high-load (long-crack) region; that is, the coarser structure has an enhanced flaw tolerance. This behaviour is typical of bridging ceramics, and reflects an inherent grain-size effect in the toughness characteristic [26]. In the present case the crossover is not pronounced, reflecting a relatively small (factor of four) change in the grain size.

3.2. Observations of Hertzian contact damage

Preliminary Hertzian contact tests using a sphere of radius $r = 1.98$ mm on silicon nitride with metal-coated surfaces revealed the presence of permanent depressions at peak loads above $P \approx 1000$ N. The surface radius of these impressions was typically $a \approx 200$ μm, corresponding to an indentation strain of $a/r \approx 0.10$ and indentation stress (contact pressure) $p_0 = P/\pi a^2 \approx 8.0$ GPa [14, 22, 27]. Thus, relative to traditional fracture testing methodologies, the Hertzian test generates uncommonly high stresses over uncommonly small sample areas [14]. It is not difficult to imagine the production of a severe, localized damage zone under such extreme stressing conditions.

Half-surface and section views of the damage in single-cycle loading are shown for the fine-grained and coarse-grained silicon nitrides in Fig. 4, at a common peak load at $P \approx 4000$ N. These views imply a certain competition between deformation and fracture processes. The surface views (Fig. 4a and c) reveal a central depression surrounded by traces of apparent cone cracks in both materials. These traces generally followed intergranular paths. It might be concluded from these surface views alone that the deformation/fracture trade-off is barely affected by microstructural differences. The cross-section views (Fig. 4b and d), on the other hand, reveal a strong microstructural influence. In the fine-grained material (Fig. 4b) the cone cracks propagate downwards and outwards into the specimen in the classical Hertzian geometry [18, 28]. The accompanying deformation, only faintly visible in this material, is confined to a zone beneath the contact area. In the coarse-grained material (Fig. 4d) no downward penetration of the surface ring cracks is detectable in the cross-section view – the macroscopic fracture characteristic is suppressed. At the same time, the damage zone appears to be much more intense, indicating enhancement of the deformation component. A

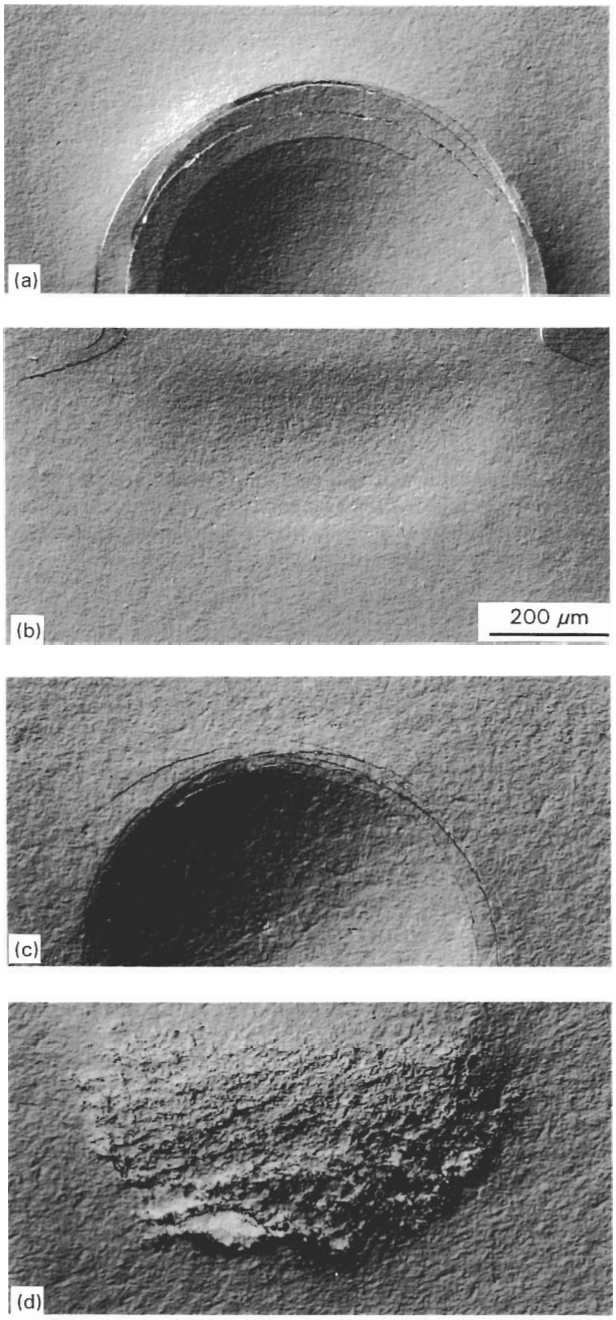

Figure 4 Optical micrographs in Nomarski interference illumination showing single-cycle Hertzian contact damage: in fine-grained (0.5 μm) silicon nitride, (a) half-surface view and (b) cross-section view; and in coarse-grained silicon nitride (c) half-surface view and (d) cross-section view. Indentations were made with a tungsten carbide sphere of radius $r = 3.18$ mm at load $P = 4000$ N (pressure $p_0 = 11.0$ GPa).

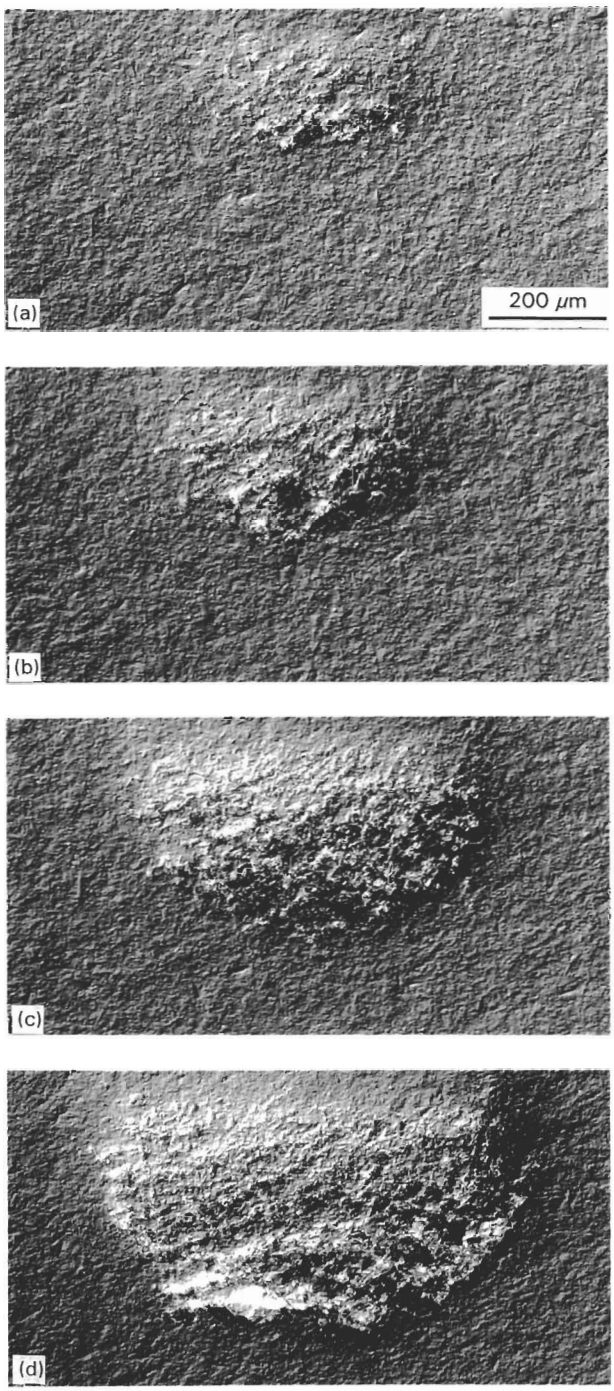

Figure 5 Optical micrographs in Nomarski interference illumination showing single-cycle Hertzian contact damage in coarse-grained silicon nitride, for indentation loads: (a) $P = 1500$ N, (b) 2000 N, (c) 3000 N, and (d) 4000 N. (Micrograph in (d) is same as Fig. 4(d).)

distinctive feature of the damage zone in both materials is the appearance of a featureless near-surface region immediately below the contact; the damage appears to be truly subsurface in nature.

The cross-section views in Fig. 5 show the progressive evolution of the subsurface damage zone with increasing single-cycle load in the coarse-grained material. Observe at the lowest load how the deformation initiates discretely below the contact surface, and progressively expands in scale and increases in intensity down the sequence until, at the highest load, it develops into a quasi-continuous zone. Again, the featureless near-surface region is a distinctive element in the micrographs.

An analogous sequence in Fig. 6 reveals the progressive evolution of damage as a function of number of cycles, at a fixed peak load $P = 2000$ N, again in the coarse-grained material. The damage intensity and zone size clearly increase down the sequence. Since hot-pressed silicon nitride has no detectable susceptibility to slow crack growth, the source of the fatigue would appear to be attributable to a true mechanical degradation process in the deformation micromechanics.

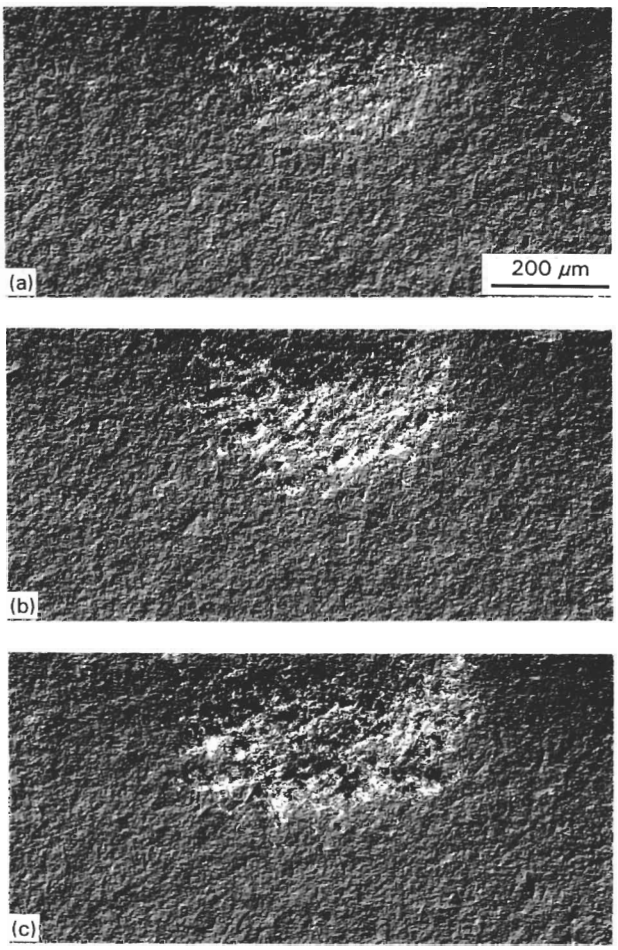

Figure 6 Optical micrographs in Nomarski interference illumination showing multiple-cycle Hertzian contact damage in coarse-grained silicon nitride, at fixed load $P = 2000$ N, for: (a) $n = 1$ cycle, (b) $n = 100$ cycles, and (c) $n = 1000$ cycles.

Fig. 7 shows SEM micrographs of the microstructure in the coarse-grained material, taken from near the centre of the subsurface damage zone in Fig. 4d. These micrographs confirm the presence of residual secondary phases at the triple-point junctions within the elongate grain structure. Copious microcracking is apparent at the grain boundaries. Note also the presence of linear, parallel traces within some of the grains. These linear *shear-fault* traces will subsequently be identified as potential sources of the microcrack initiation.

No analogous microfracture damage could be detected in the fine-grained material.

3.3. Thermal-wave observations of Hertzian contact damage

Surface and cross-section thermal-imaging scans of single-cycle damage patterns in the two silicon nitride materials are shown in Figs 8 and 9. The scans are from the same subsurface indentations shown in Figs 4 and 5. In each image the pixel size ~ 15 μm reflects the scan step size, limited by time constraints on the data accumulation. The scan data represented in these images have been smoothed by a computer processing algorithm to eliminate artefacts, such as edge scattering of the heating beam [25].

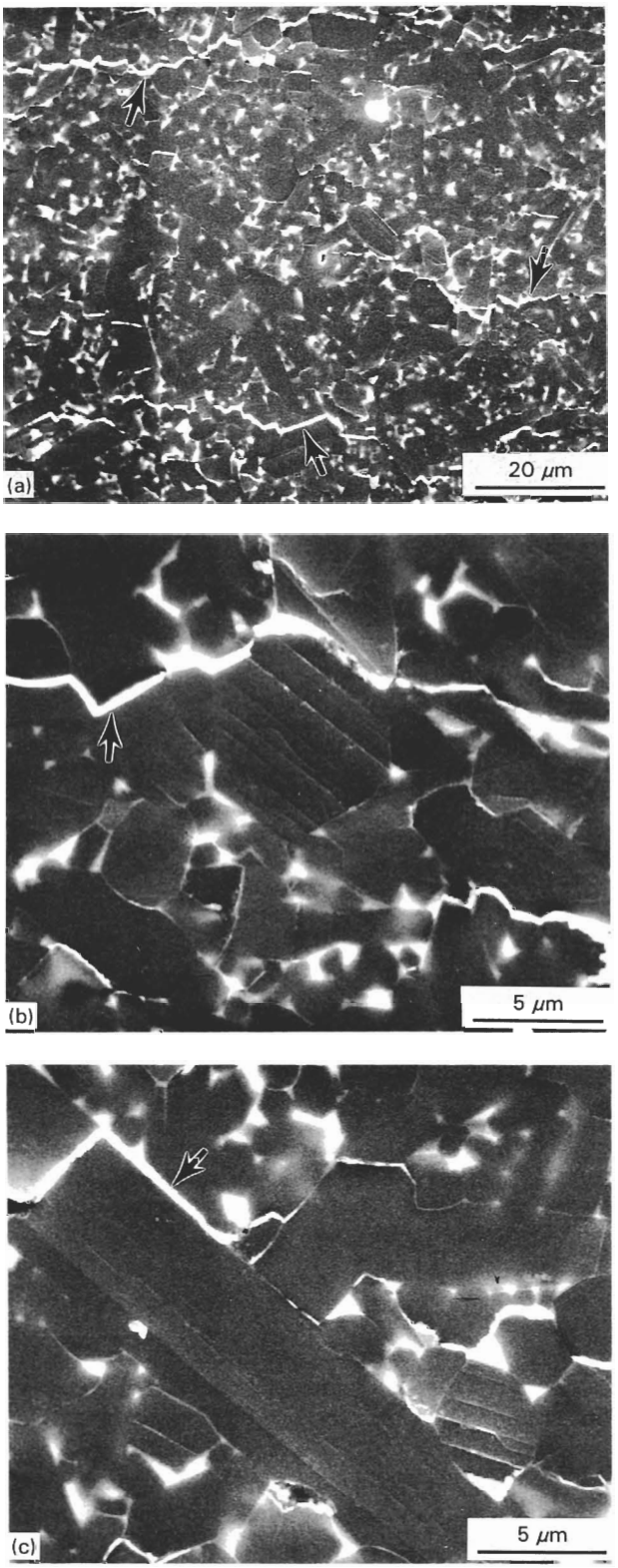

Figure 7 Scanning electron micrographs from the centre damage area of coarse-grained silicon nitride shown in Fig. 5b: (a) view showing extensive grain boundary microfracture (arrows); (b) higher magnification view, showing intergranular microfracture (arrows) and traces of intragranular slip (shear faults) within the grain at centre (grain-boundary phases are evident at the triple points); (c) similar to (b) but showing elongate grains.

In comparison with the optical micrographs in Figs 4 and 5, the thermal images show some striking correspondences and some revealing differences. The surface scans of both the fine-grained and coarse-grained materials, Figs 8a and c, show strong image

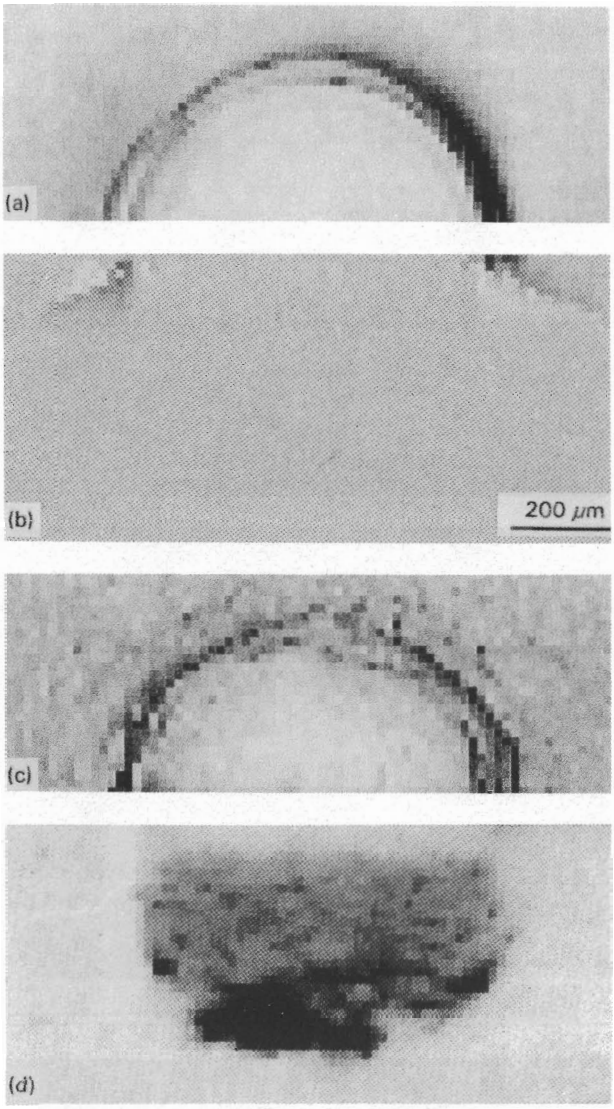

Figure 8 Thermal-wave images of single-cycle indentations shown in Fig. 4: for the fine-grained silicon nitride, (a) half-surface view and (b) cross-section view; for the coarse-grained silicon nitride, (c) half-surface view and (d) cross-section view.

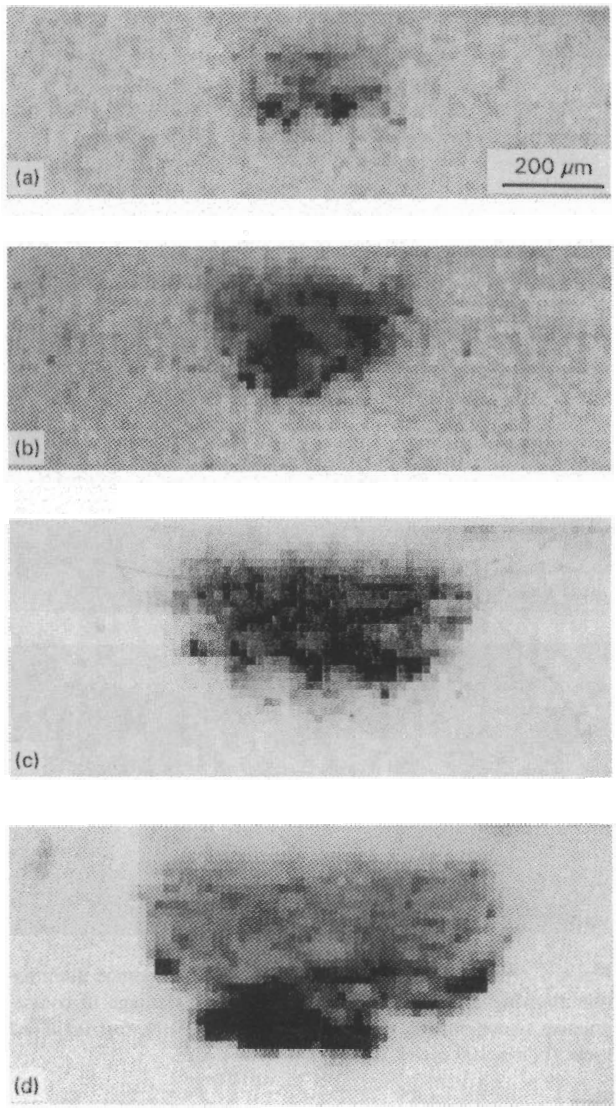

Figure 9 Thermal-wave images of single-cycle cross-section views of coarse-grained silicon nitride shown in Fig. 5: (a) $P = 1500$ N, (b) 2000 N, (c) 3000 N and (d) 4000 N.

contrast from the circular cone crack traces. At the same time, there is no enhanced contrast at all *within* the contact area, despite clear evidence of surface depressions in the optical micrographs. Hence, reliance on thermal-wave imaging of the surface alone provides a very incomplete picture of the subsurface damage pattern.

To obtain the complete picture the cross-section views in Fig. 8 and in Fig. 9 must also be considered. It is there that the indications of microstructural differences are most compellingly apparent. In the fine-grained section of Fig. 8b the traces of the penetrating cone crack are plainly visible. Again, no subsurface damage zone is detectable, even though the optical microscopy (Fig. 4a) clearly shows that such a zone exists. In the coarse-grained section of Fig. 8d, there is no sign of any cone fracture, consistent with optical observation that the surface ring cracks (Fig. 4c) are suppressed in their downward propagation (Fig. 4d). Now, however, that dramatically enhanced scattering is seen in the subcontact zone. In this context, recall from the SEM studies (Section 3.2) that microcracks are clearly detectable in the coarse-grained material but not in the fine-grained material. Again, note that the damage zone in Fig. 9 does not extend back to the surface, and that its interface with the surrounding elastic matrix is diffuse; this explains the absence of thermal-wave scattering within the contact area in the surface scan in Fig. 8c.

An issue that arises here in relation to the facility of thermal waves to image contact damage is that of artefacts from associated surface offsets at the bonded interface. To allay this concern, additional images were obtained from the same specimen used in Fig. 8c but after polishing away ~ 5 μm the cross-section surfaces. No detectable differences in the patterns could be discerned.

It may be concluded, therefore, that the experimental conditions used in the experimental set-up in Fig. 2 are highly sensitive to cracks, but are not at all sensitive to the defects that constitute the plasticity component of the damage. Free crack interfaces pro-

vide the most effective sources of phonon scattering [29]. As such, thermal-wave imaging affords a powerful methodology which, in conjunction with more traditional optical microscopy, enables distinctions to be made between the basic types of contact damage.

Thermal-wave measurements also provide a basis for quantitative evaluations of the damage, via local diffusivity measurements. In this mode, the heating beam in Fig. 2 is focused at three points within each of the subsurface damage zones in Fig. 5, and the local diffusivity at each point is deconvoluted from a scan profile by the probe beam [25]. The evaluated diffusivity data show considerably larger scatter at the smaller indentations, because of the greater spatial gradients there. Dummy runs with the beam focused on areas well away from the damage zone provide a reference baseline for data comparison.

For the fine-grained material, no difference in diffusivity could be detected between the central subsurface damage region and the remote undeformed area, at any contact load; this is consistent with the absence of subsurface deformation contrast in Fig. 8a. For the coarse-grained material, however, differences were manifest. The diffusivity data points in Fig. 10 fall steadily below the undeformed reference level (horizontal dashed line) with increasing load, consistent with a progressively increasing intensity of microfracture damage. This intensity may be quantified using a relationship [30] for the thermal conductivity, K, of a solid with randomly oriented penny cracks of radius c and number density N, making use of the proportionality between conductivity and diffusivity;

$$K = K_0/(1 + 8Nc^3/9) \qquad (1)$$

where K_0 is the conductivity in the undeformed solid. Using the data in Fig. 10, the composite term Nc^3 is calculated as a measure of the damage density; the results are plotted in Fig. 11. The solid curve through the data points is an empirical fit. Extrapolation of this curve indicates a load threshold of $\sim$1000 N, consistent with experimental observation.

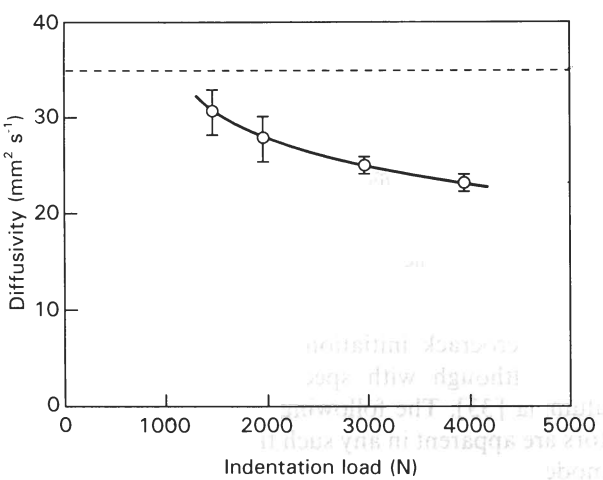

Figure 10 Local thermal diffusivity of coarse-grained silicon nitride, measured at the central region of damage-zone sections in Fig. 5, as a function of peak indentation load. Data show means and extreme values for three measurements at each indentation. Horizontal dashed line is reference baseline from measurements at remote, undeformed area.

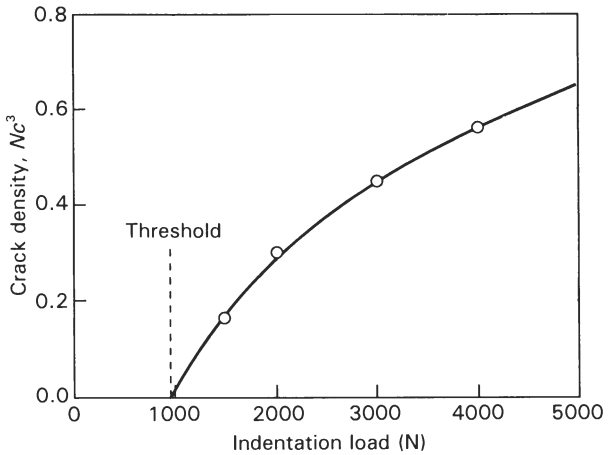

Figure 11 "Intensity" of microcrack damage, Nc^3, as a function of peak indentation load, computed from data in Fig. 10 using Equation 1.

4. Discussion

The results of our comparative study on fine-grained (0.5 μm grain size) and coarse-grained (2.0 μm) silicon nitrides demonstrate a profound influence of microstructural scale on the mechanical response in high-stress contacts. This influence is manifest in the tendency for the indentation–strength curves to cross in Fig. 3. Such crossovers, common in non-transforming ceramics [17, 26], signal an inverse relation between long-crack and short-crack toughness [23]. They represent an intrinsic competition between the resisting forces of grain bridging in the long-crack region and the driving forces of tensile grain-facet stresses in the short-crack region [4, 5]. Thus, a strong element of compromise exists in the tailoring of properties in such ceramic systems.

The long-crack/short-crack dichotomy in relation to microstructural scale in silicon nitride is even more dramatically illustrated in the optical and thermal-wave micrographs in Figs 4–9. A fundamental brittle–ductile transition is observed in the Hertzian-contact fracture response, from a macroscopic tension-driven cone crack in the fine material [18, 28, 31] to a distributed shear-driven damage zone in the coarse material [32, 33]. An intrinsic grain-size effect is implicit here, since most other elements of the silicon nitride microstructure that might otherwise have a bearing on the toughness properties, e.g. interface energy and residual stress level, are not expected to vary significantly in our two materials. As indicated in Section 1, earlier workers [19–21], using conical indenters, have noted changes in the subsurface damage patterns in various silicon nitrides, but without any reference to the kind of microstructurally associated brittle–ductile transition implied here. Again, the present use of spherical indenters is crucial to the elucidation of such transitions, to enable the mechanisms of damage evolution to be investigated in a well-defined and controllable contact stress field [14].

Generic descriptions of the subsurface damage initiation within the Hertzian contact field are now available [14–17]. As indicated, the subsurface damage evolves in a region of high shear stress beneath the

contact area. This is also a region of high hydrostatic compression, so ordinary tensile fractures are suppressed. Instead, microcracks apparently generate at the edges of constrained, *closed shear faults* in the microstructure, in the manner of mode II shear microfractures in rocks under confined pressures [34, 35]. The shear faults are closed under the action of normal compressive stresses during the faulting process, so internal friction forces restrain the sliding fault surfaces. Defining a net shear stress on the fault plane as [16]

$$S = |\tau_F| - \mu|\sigma_F| \qquad (2)$$

where τ_F and σ_F are the local shear and compression components and μ is the coefficient of sliding friction, the condition for interfacial sliding is $S > 0$. Distributions of S within the Hertzian field are plotted in Fig. 12 [16]. It is this stress that governs microcrack initiation, notwithstanding the fact that the ensuing off-plane extensions within the local stress concentrations at the fault edges will sustain a significant mode I component (*extensile* microcracks) [33, 36, 37].

It is readily apparent from Fig. 12 that the greatest shear stresses do occur in the regions below the contact centre, consistent with a subsurface origin for the damage initiation. Note the continual suppression of S as the coefficient μ increases. In particular, note the corresponding development of a layer of near-zero S in the region of maximum closure stress immediately below the contact surfaces. This explains why in the optical micrographs of Figs 4b and d, 5 and 6 no damage is observed in the near-surface regions immediately below the contact. It also explains why in the thermal-wave-image surface view of Fig. 8c for the coarse-grained material no contrast is obtained from the underlying microcrack zone, despite the clear evidence for such a zone in the corresponding cross-section views (and despite the obvious surface impression in the optical micrograph of Fig. 4a).

The basic micromechanisms of the shear-fault process responsible for the microcrack initiation remain obscure. Fault processes have been identified in previous contact-damage studies on other materials: these include intragrain twinning in alumina [14, 32], and interphase boundary slip in mica-containing glass-ceramics [16]. In our silicon nitride, we have cited linear deformation markings within individual grains in Fig. 7 as potential sources. Transmission electron microscopy (TEM) studies of deformed silicon nitride by other workers [19] suggest that such markings may be traces of crystallographic slip. Those workers also cite grain-boundary sliding as an alternative source of faulting. In all cases the faults are associated with some kind of weak interface, most likely enhanced by strong internal stresses [38]. There is scope for more fundamental work in elucidating microstructural aspects of damage in relation to damage accumulation in silicon nitride in particular, and brittle ceramics in general.

The question how the microstructural scaling might effect a brittle–ductile transition in the contact response of our silicon nitride has still to be answered. This broad question has previously been addressed in a general fracture-mechanics model of the shear-fault/microcrack initiation process in Hertzian contacts, although with specific reference to data on alumina [33]. The following two countervailing factors are apparent in any such transition in the damage mode:

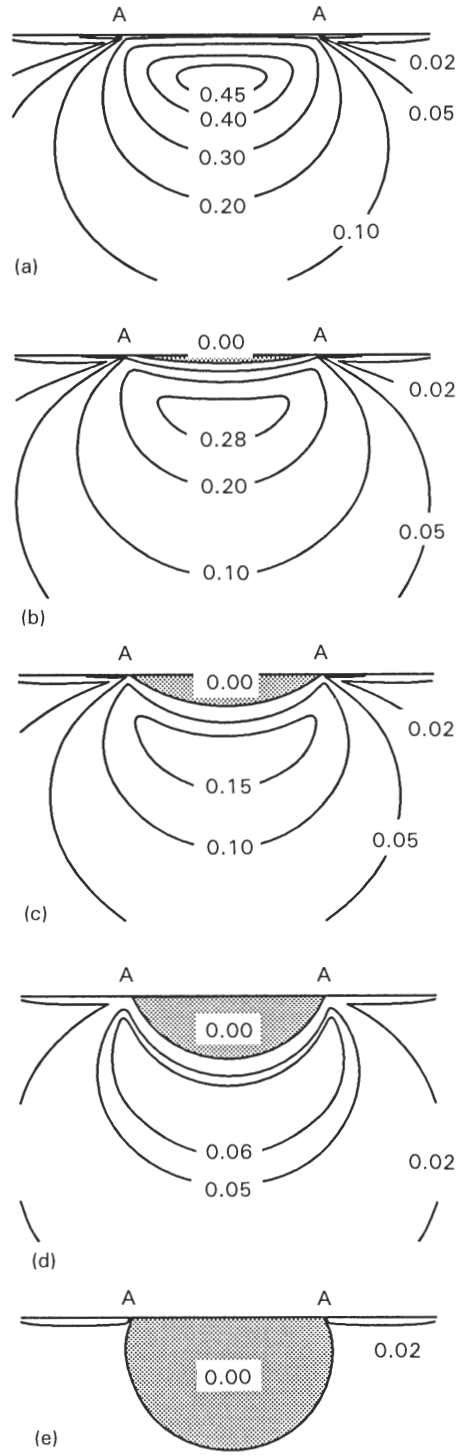

Figure 12 Contours of net shear stress, S, within the Hertzian field, for different friction coefficients, μ, in Equation 2 using Poisson's ratio of 0.27 for silicon nitride: (a) $\mu = 0.00$, (b) $\mu = 0.25$, (c) $\mu = 0.50$, (d) $\mu = 0.75$, and (e) $\mu = 1.00$. Note the strong suppression of stress levels as μ increases.

1. Cone fracture is suppressed at larger grain size, by increasing deflection of the downward propagating crack away from the principal stress trajectories that otherwise guide the extension along a direction of maximum tension [28]. Since the fracture is inter-

granular, the path deflections are greater in the coarser material, resulting in an increased tendency to crack arrest [15].

2. Subsurface microfracture in the shear zone is enhanced at larger grain size, by virtue of an increasing stress concentration at the shear-fault edges. Simplistically, treating the fault as a uniformly stressed shear crack extending over a grain dimension d [33], the stress-intensity factor scales with $d^{1/2}$. There is, therefore, a critical grain size for microcrack initiation.

Note that in our experimental study on silicon nitride we have examined a relatively small range of grain sizes, over a factor of about four. Whereas this small range usefully demonstrates the sensitivity of the contact response to microstructural scale, much more dramatic effects may be expected in extreme microstructures, e.g. in nanomaterials or in ultra coarse-grained materials.

A word may be said here concerning the relative usefulness of optical and thermal-wave imaging as a means of mapping deformation and fracture patterns in brittle ceramics. We have seen how these two techniques have different sensitivities to deformation and fracture components of the damage. In this sense the two techniques are complementary. Thus, the optical micrographs in Fig. 4 are useful for revealing the presence of both surface cone cracks and subsurface damage in the fine-grained silicon nitride; the corresponding thermal-wave images in Fig. 8a and b reveal the cone cracks, but are unable to provide any information on the presence of the subsurface zone. On the other hand, the thermal-wave images in Fig. 9 are able to distinguish the microfracture component of the subsurface damage clearly from the deformation component in the coarse-grained silicon nitride; no such unequivocal distinction is possible in the corresponding optical micrographs in Fig. 5. It should be emphasized that these distinctions are possible in the cross-sectional views only. Thus, in the special context of non-destructive evaluation, it is clear that very special care has to be taken in making deductions concerning the nature of contact damage from surface scans alone. This is of practical importance in relation to wear and machining processes, where subsurface damage always remains a threat to component integrity.

Finally, there is the issue of contact fatigue. We have done little more than foreshadow the existence of a fatigue effect in our silicon nitride. Recall from Fig. 6 the expansion of the damage zone in the coarse-grained material over 1000 cycles. Analogous cyclic damage expansion has been observed in alumina [14] and in glass–ceramics [39]. In hot-pressed silicon nitrides, the origin of any such fatigue is expected to be exclusively mechanical, owing to the virtual absence of slow crack growth. More specifically, it is attributable to attrition from internal-friction stresses at the sliding fault planes or at extensile microcrack interfaces [33]. This is another important area for further study.

Acknowledgements

The authors wish to express their gratitude to E. Lilley, G. J. Sundberg, J. W. Lucek and G. S. White for encouraging various aspects of this work and for supplying materials. H. Cai performed the stress-field calculations in Fig. 13. Support for this work was provided by the Air Force Office of Scientific Research (H. H. K. Xu and N. P. Padture) and by the Office of Intelligent Processing at NIST (L. Wei).

References

1. R. N. KATZ and J. G. HANNOOSH, *Int. J. High Technol. Ceram.* **1** (1985) 69.
2. S. J. BENNISON and B. R. LAWN, *Acta Metall.* **37** (1989) 2659.
3. N. P. PADTURE, PhD thesis. Lehigh University, Bethlehem, PA, USA (1991).
4. B. R. LAWN, N. P. PADTURE, L. M. BRAUN and S. J. BENNISON, *J. Amer. Ceram. Soc.* **76** (1993) 2235.
5. N. P. PADTURE, J. L. RUNYAN, S. J. BENNISON, L. M. BRAUN and B. R. LAWN, *ibid.* **76** (1993) 2241.
6. R. STEINBRECH, R. KNEHANS and W. SCHAAWACHTER, *J. Mater. Sci.* **18** (1983) 265.
7. P. L. SWANSON, C. J. FAIRBANKS, B. R. LAWN, Y.-W. MAI and B. J. HOCKEY, *J. Amer. Ceram. Soc.* **70** (1987) 279.
8. P. L. SWANSON, in "Fractography of glasses and ceramics", Vol. 22 edited by V. Frechette and J. Varner (American Ceramic Society, Columbus, OH, 1988), p. 135.
9. Y.-W. MAI and B. R. LAWN, *J. Amer. Ceram. Soc.* **70** (1987) 289.
10. R. F. COOK, *Acta Metall.* **38** (1990) 1083.
11. R. W. STEINBRECH, A. REICHL and W. SCHAARWÄCHTER, *J. Amer. Ceram. Soc.* **73** (1990) 2009.
12. C.-W. LI and J. YAMANIS, *Ceram. Engng. Sci. Proc.* **10** (1989) 632.
13. C.-W. LI, D.-J. LEE and S.-C. LUI, *J. Amer. Ceram. Soc.* **75** (1992) 1777.
14. F. GUIBERTEAU, N. P. PADTURE, H. CAI and B. R. LAWN, *Phil. Mag. A* **68** (1993) 1003.
15. F. GUIBERTEAU, N. P. PADTURE and B. R. LAWN, *J. Amer. Ceram. Soc.* **77** (1994) 1825.
16. H. CAI, M. A. STEVENS KALCEFF and B. R. LAWN, *J. Mater. Res.* **9** (1994) 762.
17. N. P. PADTURE and B. R. LAWN, *J. Amer. Ceram. Soc.* (in press)
18. B. R. LAWN, "Fracture of brittle solids" (Cambridge University Press, Cambridge, 1993).
19. H. MAKINO, N. KAMIYA and S. WADA, *J. Mater. Sci. Lett.* **7** (1988) 475.
20. *Idem.* in Proceedings of the 1st International Symposium on the Science of Engineering Ceramics, edited by S. Kimura and K. Niihara, (Koda, Aichi-Prefecture, Japan, 1991) p. 229.
21. H. MAKINO, N. KAMIYA and S. WADA, *J. Amer. Ceram. Soc.* **74** (1991) 2001.
22. D. TABOR, "Hardness of metals" (Clarendon, Oxford, 1951).
23. L. M. BRAUN, S. J. BENNISON and B. R. LAWN, *J. Amer. Ceram. Soc.* **75** (1992) 3049.
24. A. C. BOCCARA, D. FOURNIER and J. BADOZ, *Appl. Phys. Lett.* **36** (1980) 130.
25. L. WEI, PhD thesis. Wayne State University, Detroit, Michigan (1993).
26. P. CHANTIKUL, S. J. BENNISON and B. R. LAWN, *J. Amer. Ceram. Soc.* **73** (1990) 2419.
27. M. V. SWAIN and B. R. LAWN, *Physica Status Solidi* **35** (1969) 909.
28. F. C. FRANK and B. R. LAWN, *Proc. Roy. Soc. Lond. A* **299** (1967) 291.
29. C. KITTEL, "Introduction to Solid State Physics" (John Wiley, New York, 1967).
30. D. P. H. HASSELMAN, *J. Compos. Mater.* **12** (1978) 403.
31. B. R. LAWN and T. R. WILSHAW, *J. Mater. Sci.* **10** (1975) 1049.
32. F. GUIBERTEAU, N. P. PADTURE and B. R. LAWN (unpublished work).
33. B. R. LAWN, N. P. PADTURE, F. GUIBERTEAU and H CAI, *Acta Metall.* **42** (1994) 1683.

34. J. C. JAEGER and N. G. W. COOK, "Fundamentals of Rock Mechanics" (Chapman and Hall, London, 1971).
35. M. S. PATERSON, "Experimental Rock Deformation–The Brittle Field" (Springer-Verlag, Berlin, 1978).
36. H. HORII and S. NEMAT-NASSER, *J. Geophys. Res.* **90** (1985) 3105.
37. M. F. ASHBY and S. D. HALLAM, *Acta Metall.* **34** (1986) 497.
38. H. CAI, N. P. PADTURE, B. M. HOOKS and B. R. LAWN, *J. Europ. Ceram. Soc.* **13** (1994) 149.
39. H. CAI, M. A. S. KALCEFF, B. M. HOOKS, B. R. LAWN and K. CHYUNG, *J. Mater. Res.* **9** (1994) 2654.

Received 23 February
and accepted 10 May 1994